

Three-dimensional electronic structures and the metal-insulator transition in Ruddlesden-Popper iridates

A. Yamasaki,^{1,*} H. Fujiwara,² S. Tachibana,² D. Iwasaki,³ Y. Higashino,³ C. Yoshimi,³ K. Nakagawa,³ Y. Nakatani,² K. Yamagami,² H. Aratani,² O. Kirilmaz,⁴ M. Sing,⁴ R. Claessen,⁴ H. Watanabe,⁵ T. Shirakawa,⁶ S. Yunoki,⁶ A. Naitoh,⁷ K. Takase,⁷ J. Matsuno,⁶ H. Takagi,^{8,9} A. Sekiyama,² and Y. Saitoh¹⁰

¹Faculty of Science and Engineering, Konan University, Kobe 658-8501, Japan

²Graduate School of Engineering Science, Osaka University, Toyonaka, Osaka 560-8531, Japan

³Graduate School of Natural Science, Konan University, Kobe 658-8501, Japan

⁴Physikalisches Institut and Röntgen Center for Complex Material Systems (RCCM), Universität Würzburg, D-97074 Würzburg, Germany

⁵Waseda Institute for Advanced Study, Shinjuku, Tokyo 169-8050, Japan

⁶RIKEN Center for Emergent Matter Science (CEMS), Wako, Saitama 351-0198, Japan

⁷College of Science and Technology, Nihon University, Chiyoda, Tokyo 101-8308, Japan

⁸Department of Physics, University of Tokyo, Tokyo 113-0033, Japan

⁹Max-Planck-Institute for Solid State Research, D-70569 Stuttgart, Germany

¹⁰Materials Science Research Center, Japan Atomic Energy Agency, SPring-8, Hyogo 679-5148, Japan

In this study, we systematically investigate 3D momentum($\hbar k$)-resolved electronic structures of Ruddlesden-Popper-type iridium oxides $\text{Sr}_{n+1}\text{Ir}_n\text{O}_{3n+1}$ using soft-x-ray (SX) angle-resolved photoemission spectroscopy (ARPES). Our results provide direct evidence of an insulator-to-metal transition that occurs upon increasing the dimensionality of the IrO_2 -plane structure. This transition occurs when the spin-orbit-coupled $j_{\text{eff}}=1/2$ band changes its behavior in the dispersion relation and moves across the Fermi energy. In addition, an emerging band along the $\Gamma(0,0,0)$ - $\text{R}(\pi,\pi,\pi)$ direction is found to play a crucial role in the metallic characteristics of SrIrO_3 . By scanning the photon energy over 350 eV, we reveal the 3D Fermi surface in SrIrO_3 and k_z -dependent oscillations of photoelectron intensity in $\text{Sr}_3\text{Ir}_2\text{O}_7$. In contrast to previously reported results obtained using low-energy photons, folded bands derived from lattice distortions and/or magnetic ordering make significantly weak (but finite) contributions to the k -resolved photoemission spectrum. At the first glance, this leads to the ambiguous result that the observed k -space topology is consistent with the unfolded Brillouin zone (BZ) picture derived from a non-realistic simple square or cubic Ir lattice. Through careful analysis, we determine that a superposition of the folded and unfolded band structures has been observed in the ARPES spectra obtained using photons in both ultraviolet and SX regions. To corroborate the physics deduced using low-energy ARPES studies, we propose to utilize SX-ARPES as a powerful complementary technique, as this method surveys more than one whole BZ and provides a panoramic view of electronic structures.

PACS numbers: 74.25.Jb, 71.70.Ej, 71.20.-b, 71.30.+h

I. INTRODUCTION

Spin-orbit coupling (SOC) of an electron, a relativistic quantum effect, results in various exotic phenomena and has recently opened up new frontiers in solid state physics. Apart from the phenomena related to surface science, such as the Rashba and quantum spin Hall effects [1, 2], there are some cases in which SOC plays a predominant role in the bulk nature of condensed matter. Among them, Ruddlesden-Popper-type iridium oxides (RP-iridates) $\text{Sr}_{n+1}\text{Ir}_n\text{O}_{3n+1}$ offer an excellent opportunity for studying the interplay between the SOC and electron correlation effects in the bulk material, since the strength of the electron correlation changes together with the dimensionality of the IrO_2 -plane structure depending on the number n [3, 4].

Two-dimensional layered Sr_2IrO_4 ($n=1$; Sr214), which contains an isolated single IrO_2 plane, has the strongly spin-orbit-coupled $J_{\text{eff}}=1/2$ state, in which Ir 5d levels are partially occupied by electrons (where J_{eff} stands for the *resultant* effective total angular momentum) [5, 6]. Following are some salient features of this state: (1) the SOC in the Ir 5d electrons has an energy scale comparable to that of hopping integrals of 5d electrons and the d - d Coulomb interaction because of the large atomic number Z ($=77$). This leads to a significant splitting of Ir 5d t_{2g} levels. The five 5d electrons occupy the upper $j_{\text{eff}}=1/2$ and lower $j_{\text{eff}}=3/2$ states (where j_{eff} stands for the *one-electron* effective total angular momentum). The j_{eff} states are represented as linear combinations of atomic t_{2g} orbitals with a mixture of up and down 5d electron spins; (2) the half-filled $j_{\text{eff}}=1/2$ band, which plays an important role in the unique nature of Sr214, further splits into two bands across the Fermi energy (E_F) because of antiferromagnetic and d - d Coulomb interactions, whereas the $j_{\text{eff}}=3/2$ bands are fully occupied and lie below E_F . The presence of the half-filled insulating band

*Author to whom correspondence should be addressed.
E-mail: yamasaki@konan-u.ac.jp

(the so-called lower Hubbard band) indicates that Sr214 is a promising candidate for the parent material of high- T_c superconductors, in analogy with La_2CuO_4 [7–9]. In contrast, the final member of the system, SrIrO_3 ($n=\infty$; Sr113) shows metallic behavior above ~ 150 K [4, 10]. Sr113 is now attracting much attention because a bulk semi-metallic ground state with a new topological phase has been proposed on the basis of several theoretical studies [11–15]. In fact, the semi-metallic behavior of the Hall coefficient and possible Dirac-like linear dispersions in the electronic structures projected onto the 2D momentum (or wave number k) space were reported [4, 16, 17]. Between Sr214 and Sr113, an insulator-to-metal transition occurs with increasing dimensionality. The antiferromagnetic insulator $\text{Sr}_3\text{Ir}_2\text{O}_7$ ($n=2$; Sr327) is located close to the border of the transition [4, 18].

In the present study, we integrate the evolution of 3D electronic structures with the dimensionality of the IrO_2 -plane structure, and the synergy effects that occur between the SOC and electron correlations in J_{eff} ground states in the RP-iridates Sr214, Sr327, and Sr113. To address these issues, we use angle-resolved photoemission spectroscopy (ARPES) with brilliant soft-x-ray (SX) synchrotron radiation. In the SX region, photoemission spectroscopy is suited to the investigation of electronic structures in the bulk owing to the large probing depth [19–21]. There are two more benefits in using SX-ARPES for studying Ir j_{eff} states: (1) a high Ir $5d$ -O $2p$ sensitivity ratio, which is about 60 times higher than that in the vacuum ultraviolet (VUV) region [22] and (2) a large survey area that covers more than one whole Brillouin zone (BZ) in the 3D k space. This is made possible by scanning a photoelectron acceptance angle of about 10° and a photon energy of over 350 eV [23, 24].

Consequently, we discover k -resolved electronic structures in the RP-iridates consistent with a BZ derived from a simple square or cubic Ir lattice, in contrast to the previously reported UV and VUV-ARPES results [5, 9, 16, 25, 26]. Folded bands attributed to lattice distortions and/or magnetic ordering give significantly weak (but finite) contributions to the spectrum as a result of a matrix element effect dominant in the SX region. Through careful analysis, we conclude that a superposition of the folded and unfolded band structures has been commonly observed in ARPES experiments using photons in both UV and SX regions. Meanwhile, we successfully observe the electronic structures unique to each iridate and find direct evidence for the insulator-to-metal transition. The $j_{\text{eff}}=1/2$ band moves across E_F with increasing iridate dimensionality. Furthermore, an emerging band along the $\Gamma(0,0,0)$ -R(π,π,π) direction is shown to play a crucial role in the metallic behavior observed in Sr113.

II. EXPERIMENTAL

Thin films of pseudo-cubic perovskite-type Sr113 were grown on Nb(0.05 wt%)-doped SrTiO_3 (001) substrates by pulsed laser deposition (PLD). The typical film thickness and out-of-plane (in-plane) lattice constant were determined to be 240 Å and 3.985 (3.905) Å, respectively, using x-ray diffraction (XRD) measurements, indicating the in-plane epitaxial growth on the SrTiO_3 substrate with the original cubic lattice constant of Sr113 in the out-of-plane direction. Details of the sample preparation and characterization methods have been reported elsewhere [4].

Single crystals of Sr214 and Sr327 were prepared using a flux method with SrCl_2 as the flux material. A mixture of the starting materials (SrCO_3 and IrO_2), together with the flux, was placed into Pt crucibles and heated to 1350 °C for Sr214 (1100 °C for Sr327), and was maintained for 12 h. Subsequently, the temperature was lowered to 900 °C for 50 h. After cooling, plate-like crystals were obtained. In both complexes, the typical crystal size was about 0.8 mm \times 0.6 mm \times 0.3 mm. The crystal structures were evaluated using powder XRD at the beamline BL02B2 of SPring-8. In the case of Sr214, the lattice constants a' (= $\sqrt{2}a$) and c' (= $2c$), analyzed by Rietveld method based on the space group $I4_1/acd$, were 5.4955 Å and 25.8130 Å, respectively. Meanwhile, for Sr327, the lattice constants were determined to be a' (= $\sqrt{2}a$)=5.5157(2) Å, b' ($\simeq \sqrt{2}a$)= 5.5188(2) Å, and c =20.9027(2) Å with the symmetry of $Bbeb$. The temperature dependencies of the electrical resistivity and the magnetization under 1 T were measured between 4 and 300 K using a quantum design physical property measurement system (PPMS) and a magnetic property measurement system (MPMS). Sr214 (Sr327) samples displayed an insulating character across the entire temperature range and magnetically ordered behavior below the Néel temperature, $T_N \sim 240$ K (~ 280 K), as reported previously [27–31].

SX-ARPES experiments were performed at the Japan Atomic Energy Agency (JAEA) actinide science beamline BL23SU of SPring-8 using the Gammadata-Scienta SES-2002 electron-energy analyzer and unpolarized light delivered by a twin helical undulator [32]. Films of Sr113 were prepared with and without a two-monolayer-thick SrTiO_3 capping layer. These films were stored under a high-purity N_2 gas atmosphere during travel from the PLD growth chamber to the load lock chamber in the beamline, and then transferred to the ARPES chamber under ultrahigh vacuum (UHV). At the measuring temperature $T=20$ K, it was confirmed that both films provided qualitatively similar valence-band spectra in the binding energy (E_B) range of 0-3 eV in addition to quantitatively similar analytical results with respect to the topology of the Fermi surface (FS). To obtain clean (001) surfaces for Sr214 and Sr327, single crystals were cleaved *in situ* in UHV with a base pressure better than 1×10^{-8} Pa at the measurement temperatures [33].

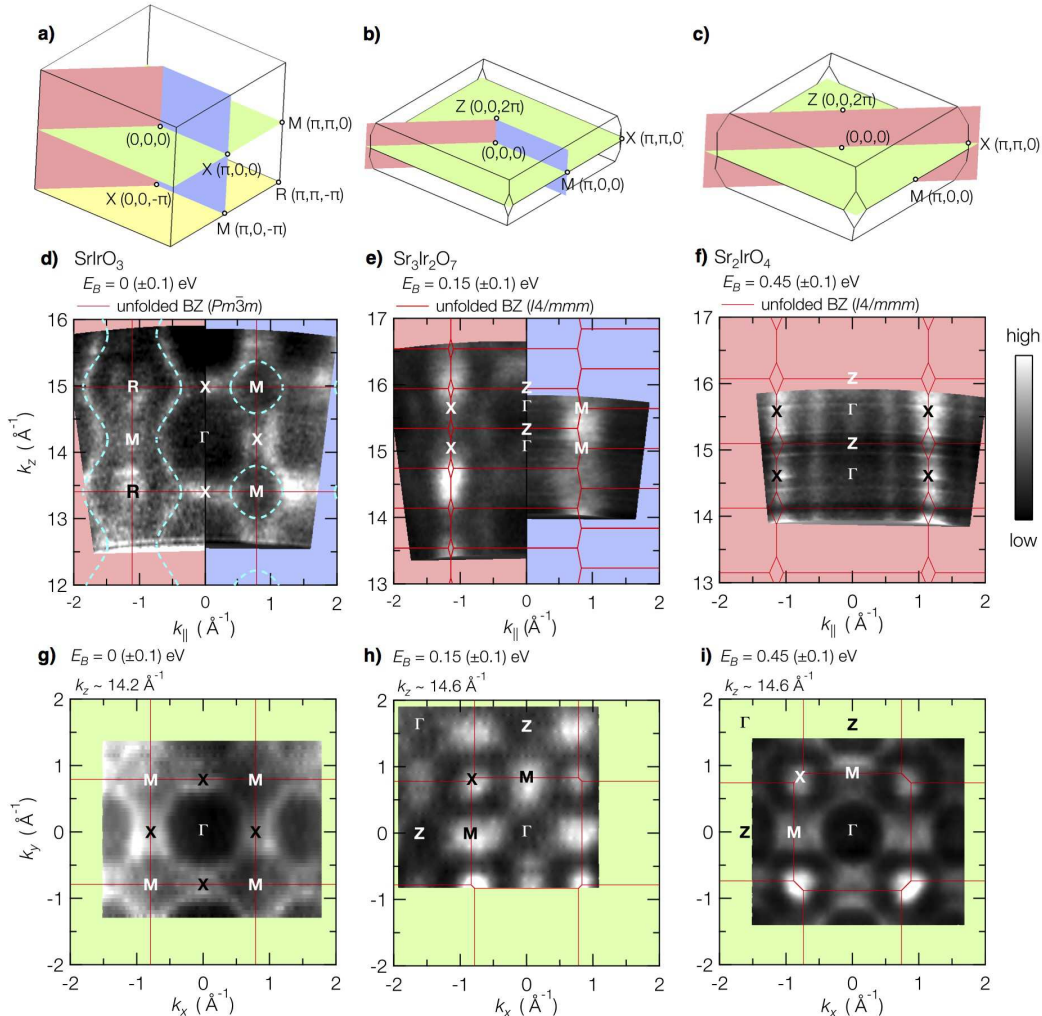


FIG. 1: Constant-energy surfaces in the \mathbf{k} space obtained using SX-ARPES. The first BZs of (a) Sr113, (b) Sr327, and (c) Sr214 for RP-type crystal structures *without* consideration of the IrO_6 octahedral rotation are shown. Note that the lattice constants a and c are omitted from the coordinate points. The constant-energy surfaces in the k_{\parallel} - k_z and k_x - k_y planes for Sr113 [(d) and (g)], Sr327 [(e) and (h)], and Sr214 [(f) and (i)] are displayed. Solid red lines indicate the cross-sectional view of the BZs illustrated in (a)-(c). Dashed curves in (d) show the cross-sectional FS discussed in Section III B. The surfaces in (d)-(i) were obtained by integrating the momentum-distribution curves around a certain E_B over an energy window of ± 100 meV [35]. Their surface topology is qualitatively similar to that with smaller energy windows under the present experimental conditions.

The energy resolution of the measurements of the energy-band dispersions along high-symmetry lines (for k -space maps) was set to about 130 (250) meV at a typical photon energy of $h\nu \simeq 750$ eV. The angular resolution was 0.2° (0.3°) parallel (perpendicular) to the analyzer slit, leading to an in-plane momentum resolution Δk_{\parallel} (or Δk_x , Δk_y) of, at most, 0.08 \AA^{-1} . Meanwhile, the momentum resolution along the k_z axis, Δk_z , was estimated to be 0.04 \AA^{-1} at the typical photon energy, which was better than one-third of Δk_z in the VUV region owing to the high bulk sensitivity in the SX region [34]. The emission angle of the photoelectron at each photon energy was converted into k_x or k_y (k_z) considering the photon mo-

mentum (and inner potential V_0 , which was experimentally estimated to be $10(\pm 3)$, $18(\pm 4)$, and $27(\pm 2)$ eV for Sr113, Sr327, and Sr214, respectively) [33]. The Fermi energy was determined from the photoemission spectra of *in situ* evaporated gold films.

III. RESULTS AND DISCUSSION

A. Overall electronic structures in RP-iridates

We show the experimentally obtained 3D k -space maps of the valence bands in RP-iridates. First, note that the

main features of k_x - k_y maps for all three iridates shown in Figs. 1(g)-(i) are consistent with the unfolded BZ picture [see also Figs. 1(a)-(c)] that were derived from crystal structures without IrO_6 octahedral rotation and/or antiferromagnetic ordering. As a result of the rotation and magnetic ordering, the space group changes from $Pm\bar{3}m$ to $Pbnm$ for Sr113, from $I4/mmm$ to $Bbeb$ for Sr327, and from $I4/mmm$ to $I4_1/acd$ for Sr214, leading to band folding and smaller BZs. However, these folded bands were less visible or, in some cases, hardly seen in the SX-ARPES (discussed later). Meanwhile, band folding in the k_x - k_y plane has been clearly observed in previous UV and VUV-ARPES experiments for the iridates [5, 9, 16, 25, 26]. These observations, which probably result from a matrix element effect, indicate that the lattice distortion and magnetic phase transition only make slight or perturbative contributions to the photoemission spectrum in the SX region. Here, we show, in a sense, the essential electronic structures expected in “undistorted” RP-iridates, whose crystal structures are similar to those of RP-ruthenates and RP-cuprates.

Cross-sectional images of the FS in Sr113 are shown in Figs. 1(d) and (g). The figures show that the $\Gamma(0,0,0)$ - $X(\pi,0,0)$ - $M(\pi,0,\pi)$ - $X(0,0,\pi)$ surface in the k_{\parallel} - k_z plane is equivalent to the $\Gamma(0,0,0)$ - $X(\pi,0,0)$ - $M(\pi,\pi,0)$ - $X(0,\pi,0)$ surface in the k_x - k_y plane, which is consistent with the cubic BZ. This result demonstrates that, in the k_z direction, vital momentum broadening and other matrix element effects were not observed. Meanwhile, in the case of Sr327, an incommensurate periodicity with the BZ along the k_z axis is seen [Fig. 1(e)], while a k_z -independent constant-energy surface has been found for Sr214, as can be expected from the strong two-dimensionality of the electronic states derived from the single-layer perovskite structure.

Turning to Fig. 2, we show the evolution of the $j_{\text{eff}}=1/2$ band width with increasing dimensionality of the IrO_2 -plane structure. The top and bottom of the $j_{\text{eff}}=1/2$ band in Sr214 were located at M point $(\pi,0,0)$ and Γ point $(0,0,0)$, respectively, as shown in Fig. 2(a). Upon changing the structure of the IrO_2 planes from 2D (Sr214), through quasi-2D (Sr327), to 3D (Sr113), the $j_{\text{eff}}=1/2$ -band width increases, as expected [Figs. 2(b)-(d)]. To understand this in more detail, the energy-band dispersions along the high-symmetry lines are shown for all RP-iridates. In the in-plane dispersions [green panels in Figs. 3(a)-(c)], the $j_{\text{eff}}=1/2$ band in Sr113 goes across the E_F along $X(\pi,0,0)$ - $M(\pi,\pi,0)$ - $\Gamma(0,0,0)$ line for Sr113 as highlighted by arrows [see also Fig. 3(d)], and forms a hole-like FS around the M point $(\pi,\pi,0)$. Meanwhile, for Sr327 and Sr214, the $M(\pi,0,0)$ - $X(\pi,\pi,0)$ - $\Gamma(0,0,0)$ line corresponding to the same path in Sr113 has its valence-band top at the M point $(\pi,0,0)$ and is folded at around $(\pi/2,\pi/2,0)$, even though the photoelectron intensity emitted from the folded band is significantly weak [see also Fig. 2(a) and 6(e)], creating a charge gap. The behavior of this band among the RP-iridates demonstrates an insulator-to-metal transition that occurs with the in-

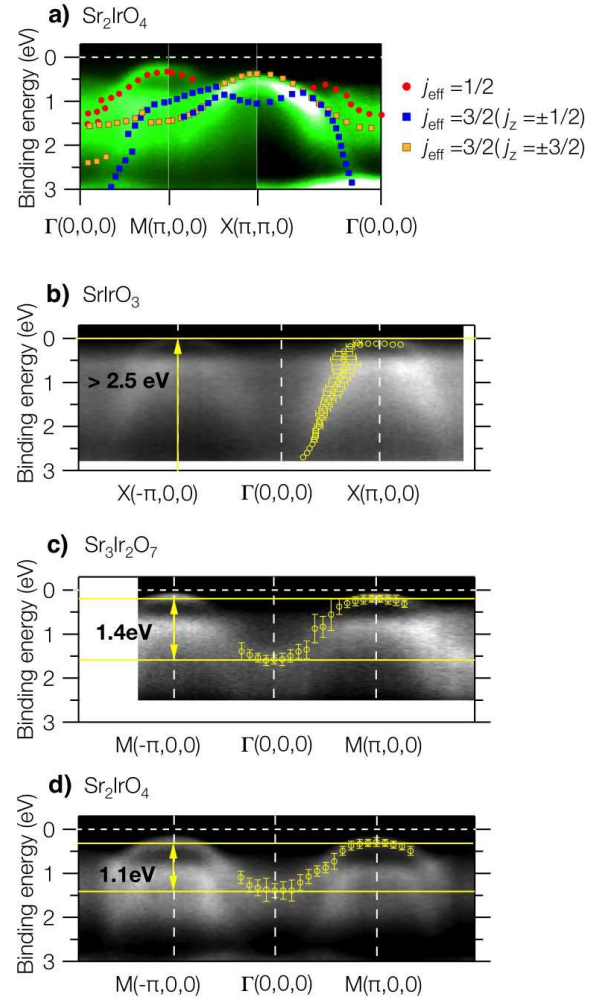


FIG. 2: $j_{\text{eff}}=1/2$ -band width depending on the dimensionality of the IrO_2 -plane structure. (a) Energy bands seen in the SX-ARPES spectra of Sr214 and the schematic view of their characters assigned by calculations (see Fig.6 for details). The $j_{\text{eff}}=1/2$ -band dispersions along the $(0,0,0)$ - $(\pi,0,0)$ line are shown for (b) Sr113, (c) Sr327, and (d) Sr214. Open circles indicate the peak positions estimated from the momentum-(energy)-distribution curves of Sr113 (Sr327 and Sr214). The error bar represents statistical variability and the variation of the peak position between the original and the second-derivative images.

crease in dimensionality associated with moving from the quasi-2D (Sr327) to the 3D (Sr113) compound.

By taking full advantage of the high- k_z resolution available in SX-ARPES, we further investigated the energy-band dispersions for all other high-symmetry lines in the 3D BZ of Sr113. Two additional E_F -crossing points were successfully observed in the $\Gamma(0,0,0)$ - $R(\pi,\pi,\pi)$ and $R(\pi,\pi,\pi)$ - $X(0,0,\pi)$ lines, as marked by arrows in the red and yellow panels in Fig. 3(a) [see also Fig. 3(d)]. The observed dispersions were compared with the results of the local density approximation (LDA)+SOC band structure calculations for cubic Sr113 with $a=3.985 \text{ \AA}$ [36, 37].

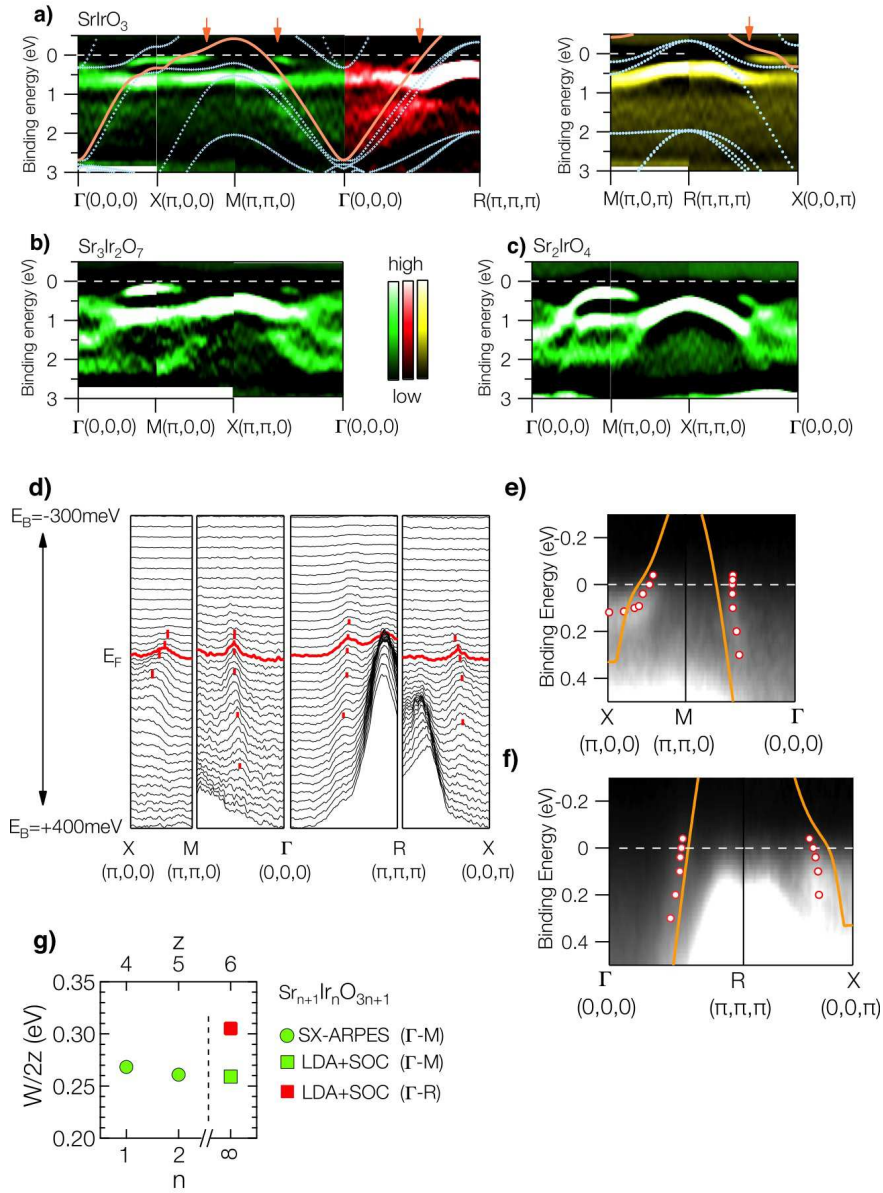


FIG. 3: Energy-band dispersions along high-symmetry lines in (a) Sr113, (b) Sr327, and (c) Sr214. To yield a better view of the dispersions, the second-derivative images are shown. The color of the images corresponds to that of the BZ planes [Figs. 1(a)-(c)], in which the high-symmetry line is included. The color of the images corresponds to that of the BZ planes [Figs. 1(a)-(c)], in which the high-symmetry line is included. The arrows in (a) indicate the positions where the observed bands go across E_F [see also (d)]. The LDA+SOC band structure of cubic Sr113 is also shown in (a). Solid orange lines indicate the $j_{\text{eff}}=1/2$ band. (d) Momentum-distribution curves of Sr113 near E_F along the high-symmetry lines, where the $j_{\text{eff}}=1/2$ band goes across the E_F . Peak positions for the momentum-distribution curves, estimated using a peak-fitting analysis, are also shown by red bars [33]. (e) and (f) Enlarged band dispersions in the vicinity of E_F . Open circles in red indicate the peak positions in either the momentum- or energy-distribution curve. Calculated $j_{\text{eff}}=1/2$ bands are shown by solid orange lines. (g) $W/2z$ value corresponding to an averaged hopping integral t in the $j_{\text{eff}}=1/2$ band, where z stands for the number of nearest-neighbor Ir atoms. Here, W for Sr214 and Sr327 is defined as $2w$, where w is the $j_{\text{eff}}=1/2$ -band width in the occupied state. The dashed line divides the insulating and metallic states.

The behavior of the $j_{\text{eff}}=1/2$ band near the E_F -crossing points was generally well-reproduced by the calculation shown in Figs. 3(e) and (f); however, some inconsistency is apparent in Fig. 3(a). Some bands, whose tops are located at the R point (π, π, π) , are pushed below E_F . In contrast, other bands around the Γ point $(0, 0, 0)$ seem to

go above E_F . These shifts make the theoretically predicted hole (electron) pockets around the R (Γ) point disappear. Since our calculated results do not have any flat band in the $M(\pi, \pi, 0)$ - $\Gamma(0, 0, 0)$, $\Gamma(0, 0, 0)$ - $R(\pi, \pi, \pi)$, and $\Gamma(0, 0, 0)$ - $X(\pi, 0, 0)$ lines, the observed bands at $E_B \simeq 0.7$ eV around the Γ point are considered to be folded

TABLE I: The experimentally and theoretically obtained gradient of the $j_{\text{eff}}=1/2$ band at E_F and the Fermi velocity in Sr113.

| | high-symmetry line in cubic BZ | $\left. \frac{dE}{dk} \right _{k=k_F}$ (eV Å) | v_F ($\times 10^7$ cm/s) |
|----------|-----------------------------------|--|--------------------------------|
| SX-ARPES | X – M | 0.8 (± 0.2) | 1.2 (± 0.3) |
| | M – Γ | > 3.0 | > 4.6 |
| | Γ – R | 3.3 (± 0.2) | 5.0 (± 0.3) |
| | R – X | 1.4 (± 0.4) | 2.2 (± 0.6) |
| LDA+SOC | X – M | 0.64 | 0.97 |
| | M – Γ | 2.5 | 3.8 |
| | Γ – R | 3.1 | 4.7 |
| | R – X | 0.92 | 1.4 |

bands resulting from the IrO_6 octahedral rotation, as seen in the $X(\pi, \pi, 0)$ - $\Gamma(0, 0, 0)$ line for Sr327 and Sr214. In fact, as mentioned above, the photoelectron intensity emitted from these bands was weaker than the original bands. Other bands that have broad bandwidths of more than 2 eV are hardly seen in Fig. 3(a); however, these bands become more visible following a change in photon energy and are reproduced by our calculations [33]. Our results suggest that the narrow j_{eff} bands observed in the low-energy ARPES experiments [16, 17] are not derived from the electron correlation effect but from lattice distortion together with the matrix element effect. Unlike the results reported in a previous study [3], we conclude that the electron correlation in Sr113 is rather weak.

B. Fermiology of SrIrO_3

Figures 3(e) and (f) show the photoelectron-intensity distributions in the vicinity of E_F around the M point $(\pi, \pi, 0)$ and R point (π, π, π) . It can be clearly seen that the $j_{\text{eff}}=1/2$ band has various slopes at the Fermi wavenumber k_F on each high-symmetry line. The estimated Fermi velocities, v_F , are listed in Table I. The value near the $(\pi/2, \pi/2, \pi)$ in the $R(\pi, \pi, \pi)$ - $X(0, 0, \pi)$ line is almost equal to the previously reported value of 1.2 eV Å at $(\pi/2, \pi/2)$ in the surface-projected BZ [16]. Furthermore, we uncovered a significantly faster band with 3.3 eV Å, that is, $v_F=5.0 \times 10^7$ cm/s near $(\pi/2, \pi/2, \pi/2)$ in the $\Gamma(0, 0, 0)$ - $R(\pi, \pi, \pi)$ line; this value is about half the value generally reported for simple metallic systems [39]. These experimentally obtained v_F values can be reproduced by the LDA+SOC calculation for cubic Sr113, also listed in Table I, supporting the dominant $j_{\text{eff}}=1/2$ character of this band in Sr113.

We now discuss the FS topology of Sr113 in detail. The $j_{\text{eff}}=1/2$ -band dispersions in Figs. 3(e) and (f) suggest the presence of two hole pockets around the M point $(\pi, \pi, 0)$ and R point (π, π, π) ; however, Fig. 1(d) shows

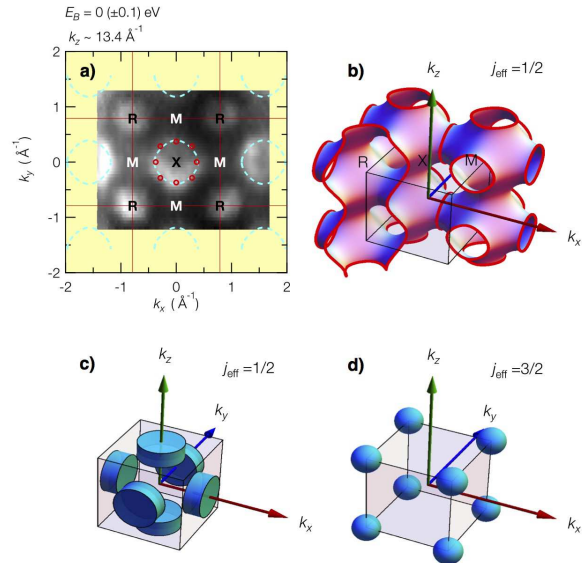


FIG. 4: FS topology of Sr113. (a) Constant-energy surface (including the FS) in the $R(\pi, \pi, \pi)$ - $M(\pi, 0, \pi)$ - $X(0, 0, \pi)$ - $M(0, \pi, \pi)$ plane. Open circles in red indicate the k_F points estimated from the ARPES spectra [33]. (b) Schematic image of a hole-like FS for a simple cubic structure is shown. The cross-sectional views of the FS are also illustrated by the dashed line in (a) and Fig. 1(d). Electron reservoirs just below E_F are displayed in (c) and (d).

that they are connected to each other along the $R(\pi, \pi, \pi)$ - $M(\pi, \pi, 0)$ line, leading to a large open FS. The experimental FS closely resembles a hole-like FS for a simple cubic structure in the tight-binding (TB) model illustrated in Fig. 4(b). The FS is composed of a simplified energy band $\epsilon_{\mathbf{k}} = -2t(\cos k_x a + \cos k_y a + \cos k_z a)$, where t is an hopping integral [40]. At $\epsilon_{\mathbf{k}} = 0$, the energy band reproduces a characteristic FS topology in the $R(\pi, \pi, \pi)$ - $M(\pi, \pi, 0)$ - $\Gamma(0, 0, 0)$ - $X(0, 0, \pi)$ plane as shown in Fig. 1(d) and the TB-model FS is consistent with the number of E_F -crossing points observed in all high-symmetry lines. Here, we roughly estimate the number of the hole n_h , not using the LDA+SOC but the TB band since the experimental k_F values are well reproduced by the TB-model calculation rather than the LDA+SOC calculation [33]. Approximating the experimental FS by the TB-model FS, n_h in the Wigner-Seitz cell can be analytically obtained by

$$n_h = 2 \frac{V_{\text{FS}}}{\left(\frac{2\pi}{a}\right)^3} = 1, \quad (1)$$

where $V_{\text{FS}} (=4\pi^3/a^3)$ is the volume of the TB-model FS. Following are the two principal results of the SX-ARPES: (1) the observed band going across E_F corresponds to

$j_{\text{eff}}=1/2$ and (2) $n_h \simeq 1$. These results suggest that Sr113 has a well-defined $J_{\text{eff}}=1/2$ ground state, as do Sr214 and Sr327. Thus, the $J_{\text{eff}}=1/2$ picture is valid independent of the dimensionality in RP-iridates. Here, note that the FS consisting of only hole-like bands appeared to be inconsistent with the strongly temperature-dependent and negative Hall coefficient and other theoretical predictions which suggest that Sr113 is semi-metallic [4, 11, 12]. In fact, it has been reported that the electron-like FS is composed of some folded bands invisible in SX-ARPES [16]. Apart from that, we observed a finite photoelectron intensity at E_F around the R and X points, as shown in Fig. 4(a) [see also Figs. 1(d) and (g)], resulting from the $j_{\text{eff}}=3/2$ and $1/2$ bands approaching E_F and a finite energy resolution. These bands form “electron reservoirs” as shown in Figs. 4(c) and (d), and can contribute to the electron conductivity at high temperature.

C. Bilayer coupling effect in $\text{Sr}_3\text{Ir}_2\text{O}_7$

Let us now discuss the dependence of the photoelectron intensity on k_z in the constant-energy surface of Sr327.

$$\begin{aligned}
 M_z(k_z) &= \int_{-\infty}^{\infty} z \exp\left[-\frac{\left(z - \frac{d}{2}\right)^2}{(\beta d)^2}\right] \exp(ik_z z) dz \pm \int_{-\infty}^{\infty} z \exp\left[-\frac{\left(z + \frac{d}{2}\right)^2}{(\beta d)^2}\right] \exp(ik_z z) dz \\
 &= \begin{cases} i\sqrt{\pi}\beta d \exp\left(-\frac{\beta^2 d^2}{4} k_z^2\right) \left\{ d \sin\left(\frac{d}{2} k_z\right) + \beta^2 d^2 k_z \cos\left(\frac{d}{2} k_z\right) \right\} & : \text{for } \chi_e(z), \\ \sqrt{\pi}\beta d \exp\left(-\frac{\beta^2 d^2}{4} k_z^2\right) \left\{ d \cos\left(\frac{d}{2} k_z\right) - \beta^2 d^2 k_z \sin\left(\frac{d}{2} k_z\right) \right\} & : \text{for } \chi_o(z), \end{cases}
 \end{aligned} \tag{2}$$

where d is the distance between IrO_2 layers, 4.070\AA [30]. The damping parameter β was set to be $1/35$ so as to reproduce the experimental results. Note that this optimal value of β is much smaller than that reported for Bi2212 ($\beta=1/6$) in the VUV-ARPES experiment, indicating the narrow spread of the wave function in the present initial state [41]. In the photoemission event using x-rays, the valence electron is considered to be emitted spatially close to the ionic core, which can result in small β values [42].

As shown in Fig. 5(b), the oscillation of the photoelectron intensity at $E_B=0.15$ eV along the X-X line in the k_z direction is well-reproduced by the calculated $M_z(k_z)$. This demonstrates that the oscillation near E_F is derived from the symmetrically coupled Ir $5d$ state [43]. The energy distribution curves along the X-X line are shown in Fig. 5(a). It was found that the peak con-

tributing to the oscillation shifts to a point corresponding to a deeper E_B when the transition probability M_z^2 for the anti-symmetrically coupled wave function $\chi_o(z)$ becomes large, as shown in Fig. 5(b). Therefore, the two peaks at $E_B \simeq 350$ and 550 meV can be assigned to the anti-bonding and bonding states, originating from $\chi_e(z)$ and $\chi_o(z)$, respectively. This is known as bilayer splitting, and the splitting energy is estimated to be about 200 meV. Bilayer splitting in the folded band was observed at the Γ point [26]. Interestingly, with changing k_z values, the strengths of the photoelectron intensities along X-X and M-M lines increase and decrease alternately [see Fig. 1(e)], indicating that the anti-bonding state at the M point is derived from χ_o instead of χ_e . Considering, as in the case of Sr214, that the $j_{\text{eff}}=1/2$ ($3/2$) band predominates in the vicinity of E_F at the M (X) point, it is clear that the nature of bilayer coupling

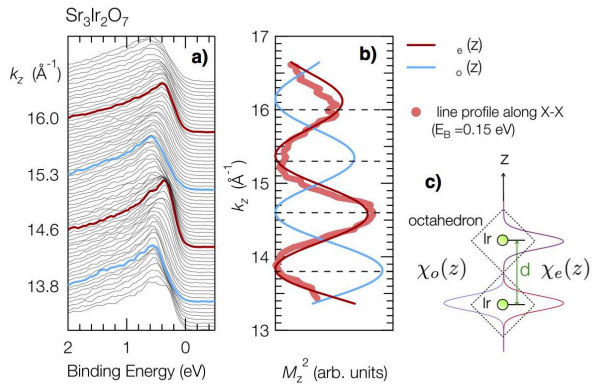


FIG. 5: Bilayer splitting and matrix element effect in Sr327. (a) Energy-distribution curves along the X-X line in the k_z direction. (b) Transition probability along the k_z axis, M_z^2 , induced by photoexcitation for a bilayer-coupled system. The photoelectron intensity along the X-X line from Fig. 1(e) is also shown. (c) Schematic illustration of the bilayer-coupled wave functions.

TABLE II: The number of j_{eff} bands at each high-symmetry point between E_F and $E_B=2\text{eV}$ in Sr214, observed using ARPES experiments at various photon energies.

| $h\nu$ | $I4/mmm$ | (0,0) | $(\pi,0)$ | $(\pi/2,\pi/2)$ | (π,π) |
|----------------------|------------|----------|-----------|-----------------|-------------|
| | $I4_1/acd$ | Γ | M | M | X |
| 760 eV | | 3 | 3 | 2 | 1 |
| 85 eV ^a | | 1 | 2 | 2 | - |
| 21.2 eV ^b | | 3 | 3 | 2 | 2 |

^aRef. [5].

^bRef. [44].

depends on the j_{eff} band character.

D. Superposition of folded and unfolded band structures in Sr₂IrO₄

Here, we provide deeper insight into the inconsistency in the expected BZ size determined by SX-ARPES and the other two experiments, UV-ARPES and XRD, by discussing the well-known electronic structure in Sr214. As has already been reported, the crystal structure of Sr214 is determined by XRD [27]. The in-plane rotation (11°) of the IrO₆ octahedra makes the primitive vectors rotate and the in-plane (out-of-plane) lattice constant a (c) expands by a factor of $\sqrt{2}$ (2), changing the crystallographic space group from $I4/mmm$ to $I4_1/acd$. As a result, Sr214 has a small folded BZ unlike that of the triplet superconductor Sr₂RuO₄. In comparison with the energy-band dispersions at $h\nu=760$ eV in Fig. 3(c) and

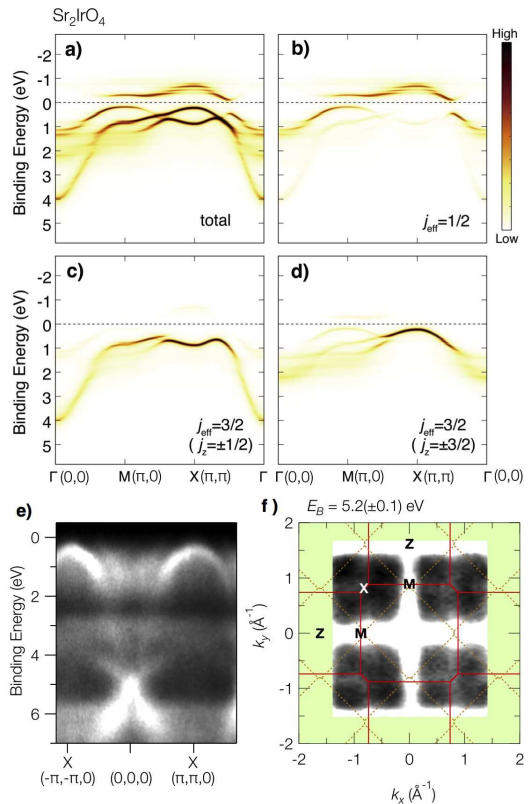


FIG. 6: (a) Theoretical energy spectrum based on the three-orbital Hubbard model with consideration for the unfolded BZ of Sr214. (b)-(d) Spectra projected onto the atomic $j_{\text{eff}}=1/2$, $3/2$ ($j_z=\pm 1/2$), and $3/2$ ($j_z=\pm 3/2$) bases, respectively. The parameters and their values for the calculation are identical to those used in the previous study (*i.e.*, $U=1.44$ eV, $U'=1.008$ eV, $J=0.216$ eV, and $\lambda=0.432$ eV in Ref. [46]). (e) Experimental energy-band dispersion along $\Gamma(0,0,0)$ - $X(\pi,\pi,0)$ line. (f) Constant-energy surface at $E_B=5.2(\pm 0.1)$ eV. These images were taken at $h\nu=760$ eV. In (f), unfolded and folded BZs are drawn as solid and dotted lines, respectively.

at 21.2 eV in Ref. [44], the overall characteristic feature of the j_{eff} bands, including the number of bands passing through the high-symmetry points listed in Table II, are in good agreement with each other. We stress that the experimental results at both photon energies can be well-reproduced by the energy spectrum calculated for the *unfolded* BZ shown in Figs. 6(a)-(d), with the expectation of the band approaching E_F near the Γ point. Meanwhile, the other band, whose bottom is located at (π,π) near $E_B=1$ eV at $h\nu=21.2$ eV, is not resolved at 760 eV but theoretically predicted within the unfolded BZ picture, as shown in Fig. 6(c) [45]. It can be seen that the exceptional band near the Γ point is derived from the band folding since it appears in the calculated spectrum for the folded BZ [46]. Nevertheless, the major feature in the k -resolved photoemission spectra obtained using both high- and low-energy photons are correctly explained within the unfolded BZ picture in Sr214 as

in other RP-iridates. This shows that, in any ARPES result, the high-symmetry point (π, π) should be distinguished from the Γ point $(0, 0)$, even though they are identical in the surface-folded BZ [47].

Furthermore, it is clear that the photoelectron-intensity ratio of the folded band relative to the other unfolded bands does not change over the range of $h\nu \simeq 400$ and 800 eV [33]. This indicates that either the folded or unfolded band is not derived from the surface structures since the probing depth changes from about 9 to 15 Å with increasing photon energy. We observed another folded band around the X point (π, π) , whose intensity is significantly weak, in the O 2*p* (and Ir 5*d* bonding) states, as shown in Fig. 6(f). Note that the unfolded band structure in the O 2*p* states remains dominant, even though the oxygen atoms change their positions due to the IrO₆ octahedral rotation. Judging from the above results, we can conclude that the weak intensity arising from the folded bands in the SX-ARPES spectra is not caused by the bulk/surface or any specific band character. We propose here that the most promising candidate for the origin of this folded/unfolded problem is the matrix element effect of the electric dipole transition in the photoemission process excited by high-energy photons. A better understanding of this phenomenon is expected to result from further theoretical studies.

E. Structural dimensionality and metal-insulator transition

Finally, we discuss the relationship among the electronic nature, structural dimensionality, and magnetic ordering in RP-iridates. Based on a simple TB model, the hopping integral t is expressed as $W/2z$, where W and z are the bandwidth and the number of nearest-neighbor Ir atoms, respectively. Figure 3(g) shows a plot of the $W/2z$ values for the $j_{\text{eff}}=1/2$ band in the $\Gamma(0,0,0)$ -M($\pi, \pi, 0$) and $\Gamma(0,0,0)$ -R(π, π, π) lines obtained from the LDA+SOC calculation for Sr113. The values in the $\Gamma(0,0,0)$ -M($\pi, 0, 0$) line of Sr214 and Sr327, estimated from the dispersions observed in Figs. 2(c) and (d), are also shown. The hopping integral in Sr113 along the $\Gamma(0,0,0)$ -M($\pi, \pi, 0$) line is nearly the same as the in-plane integrals in Sr214 and Sr327. Meanwhile, the integral has a significantly large value along the $\Gamma(0,0,0)$ -R(π, π, π) line, in which the hopping is only possible in the 3D crystal structure unique to Sr113. This fact strongly suggests that the hopping of the carrier along the body diagonal direction plays a crucial role in the metallic nature of Sr113.

In contrast to Sr113 ($n=\infty$), Sr327 ($n=2$) and Sr214 ($n=1$) have no clear Fermi cutoff in the k -integrated spectra shown in Fig. 7(a). This feature becomes more apparent at the M point $(\pi, 0, 0)$ where the $j_{\text{eff}}=1/2$ band has the valence-band top in both compounds. Figure 7(b) shows that the k -resolved spectrum of Sr327 has a prominent peak at $E_B \simeq 150$ meV below the magnetic ordering

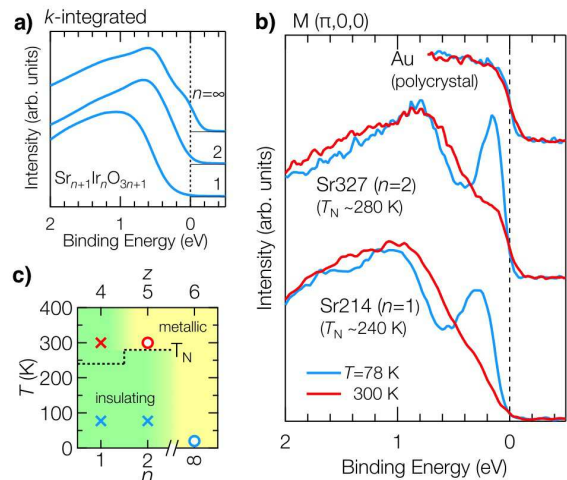


FIG. 7: Metal-insulator transition in RP-iridates. (a) k -integrated spectra of Sr113 ($n=\infty$), Sr327 ($n=2$), and Sr214 ($n=1$) obtained by summing up the SX-ARPES spectra in both k_x - k_y and $k_{||}$ - k_z planes shown in Figs. 1(d)-(i). (b) Temperature dependence of the SX-ARPES spectrum at the M point $(\pi, 0, 0)$. (c) The structural dependence of the electronic nature and its temperature variation, where z stands for the number of nearest-neighbor Ir atoms. Open circles (cross marks) indicate the temperatures at which the Fermi cutoff was (not) observed.

temperature T_N , whose tail goes across E_F to unoccupied states because of a finite energy resolution. Even though non-zero photoelectron intensity at E_F was observed, the clear Fermi cutoff could not be found in the spectrum. The peak observed below T_N becomes wider and shifts to a deeper E_B with decreasing n , *i.e.*, the structural dimensionality. The peak shift results in the creation of the charge gap in Sr214.

The k -resolved spectra of Sr327 and Sr214 above T_N , also shown in Fig. 7(b), resemble the k -integrated spectra of these compounds in Fig. 7(a), respectively, suggesting that a k -broadening effect predominates at room temperature [48]. The k broadening observed here is derived from the matrix element effect mainly related to the Debye-Waller factor [49]. In addition, the energy broadening of a few hundred meV resulting from the phonon-induced effect should be considered [50]. Despite these broadening effects, it is revealed that the k -resolved spectra of Sr327 and Sr214 in the vicinity of E_F are significantly different from each other. The Fermi cutoff in the spectrum of Sr327 appears above T_N , indicating that an insulator-to-metal transition occurs across T_N . Collapse of the charge gap consistent with the drop of the electrical resistivity above T_N demonstrates that a strong Mott insulating picture is not applicable to Sr327 [31, 51, 52]. In contrast, Sr214 has no Fermi cutoff in the k -resolved spectrum and maintains the insulating character even above T_N . Based on these results, we construct a phase diagram in which the metallic nature of RP-iridates, mediated by

the electrons in the spin-orbit coupled $j_{\text{eff}}=1/2$ band, develops step-by-step with increasing dimensionality of the IrO_2 -plane structure and with the help of magnetic ordering as summarized in Fig. 7(c).

IV. SUMMARY

We measured the 3D k -resolved electronic structures of three RP-iridates Sr113, Sr214, and Sr327, using bulk-sensitive SX photoemission spectroscopy in conjunction with theoretical calculations. The most striking results in the present study are as follows: (1) it was clearly demonstrated that the insulator-to-metal transition is induced by the variation in the $j_{\text{eff}}=1/2$ band dispersion, which occurs with the increasing dimensionality in the RP-iridates. In addition, Sr327 solely showed the transition in conjunction with the magnetic phase transition induced by temperature change. (2) We discovered a perfect 3D FS. This was made possible by the use of the synchrotron light in the scanned photon energy range of more than 350 eV. Furthermore, the dispersions among all the high-symmetry points in the cubic BZ were experimentally revealed. (3) Broadly dispersive $j_{\text{eff}}=1/2$ bands, which only go across E_F and are well-separated from $j_{\text{eff}}=3/2$ bands, can be used to categorize Sr113 as a $J_{\text{eff}}=1/2$ itinerant electron system. (4) We directly observed the photoelectron-intensity oscillation derived from the bilayer coupling and found its anisotropy in the

k space depending on the j_{eff} band character.

Note that the superposition of the folded and unfolded band structures can be intrinsically observed in the ARPES experiments using any photons from the UV to the SX region.

Acknowledgments

We would like to thank Y. Higa for supporting the SX-ARPES experiments, A. Higashiya for supporting analysis, S. Suga for careful reading of the manuscript, H. Wadati for fruitful discussions, and C. Moriyoshi and Y. Kuroiwa for the XRD measurements of Sr214 and Sr327. This work was performed under the Shared Use Program of JAEA Facilities (Proposals No. 2014A-E29, 2015A-E23, and 2015B-E23) with the approval of Nanotechnology Platform project supported by the Ministry of Education, Culture, Sports, Science and Technology (MEXT) (Proposals No. A-14-AE-0022, No. A-15-AE-0021) and JSPS Grant-in-Aid for Scientific Research (C)(No. JP15K05186). H.W., T.S., and S.Y. was supported by Grant-in-Aid for Scientific Research from MEXT Japan under the Grant No. 25287096). The synchrotron radiation experiments were performed at the JAEA beamline BL23SU (Proposals No. 2014A3882, No. 2015A3882, and No. 2015B3882) and the JASRI beamline BL02B2 (No. 2016A1230) of SPring-8.

-
- [1] Y. A. Bychkov and É. I. Rashba, *Properties of a 2D electron gas with lifted spectral degeneracy*, Pisma Zh. Eksp. Teor. Fiz. **39**, 66 (1984) [JETP Lett. **39**, 78 (1984)].
- [2] C. L. Kane and E. J. Mele, *Quantum Spin Hall Effect in Graphene*, Phys. Rev. Lett. **95**, 226801 (2005).
- [3] S. J. Moon, H. Jin, K. W. Kim, W. S. Choi, Y. S. Lee, J. Yu, G. Cao, A. Sumi, H. Funakubo, C. Bernhard, and T. W. Noh, *Dimensionality-Controlled Insulator-Metal Transition and Correlated Metallic State in 5d Transition Metal Oxides $\text{Sr}_{n+1}\text{Ir}_n\text{O}_{3n+1}$ ($n=1, 2$, and ∞)*, Phys. Rev. Lett. **101**, 226402 (2008).
- [4] J. Matsuno, K. Ihara, S. Yamamura, H. Wadati, K. Ishii, V. V. Shankar, H.-Y. Kee, and H. Takagi, *Engineering a Spin-Orbital Magnetic Insulator by Tailoring Superlattices*, Phys. Rev. Lett. **114**, 247209 (2015).
- [5] B. J. Kim, H. Jin, S. J. Moon, J.-Y. Kim, B.-G. Park, C. S. Leem, J. Yu, T. W. Noh, C. Kim, S.-J. Oh, J.-H. Park, V. Durairaj, G. Cao, and E. Rotenberg, *Novel $J_{\text{eff}}=1/2$ Mott State Induced by Relativistic Spin-Orbit Coupling in Sr_2IrO_4* , Phys. Rev. Lett. **101**, 076402 (2008).
- [6] B. J. Kim, H. Ohsumi, T. Komesu, S. Sakai, T. Morita, H. Takagi, and T. Arima, *Phase-Sensitive Observation of a Spin-Orbital Mott State in Sr_2IrO_4* , Science **323**, 1329 (2009).
- [7] H. Watanabe, T. Shirakawa, and S. Yunoki, *Monte Carlo Study of an Unconventional Superconducting Phase in Iridium Oxide $J_{\text{eff}}=1/2$ Mott Insulators Induced by Carrier Doping*, Phys. Rev. Lett. **110**, 027002 (2013).
- [8] Y. K. Kim, O. Krupin, J. D. Denlinger, A. Bostwick, E. Rotenberg, Q. Zhao, J. F. Mitchell, J. W. Allen, and B. J. Kim, *Fermi arcs in a doped pseudospin-1/2 Heisenberg antiferromagnet*, Science **345**, 187 (2014).
- [9] A. de la Torre, S. McKeown Walker, F. Y. Bruno, S. Riccò, Z. Wang, I. Gutierrez Lezama, G. Scheerer, G. Giriat, D. Jaccard, C. Berthod, T. K. Kim, M. Hoesch, E. C. Hunter, R. S. Perry, A. Tamai, and F. Baumberger, *Collapse of the Mott Gap and Emergence of a Nodal Liquid in Lightly Doped Sr_2IrO_4* , Phys. Rev. Lett. **115**, 176402 (2015).
- [10] Y. K. Kim, A. Sumi, K. Takahashi, S. Yokoyama, S. Ito, T. Watanabe, K. Akiyama, S. Kaneko, K. Saito, and H. Funakubo, *Metalorganic Chemical Vapor Deposition of Epitaxial Perovskite SrIrO_3 Films on (100) SrTiO_3 Substrates*, Jpn. J. Appl. Phys. **45**, L36 (2006).
- [11] J. M. Carter, V. V. Shankar, M. A. Zeb, and H.-Y. Kee, *Semimetal and Topological Insulator in Perovskite Iridates*, Phys. Rev. B **85**, 115105 (2012).
- [12] M. A. Zeb and H.-Y. Kee, *Interplay between spin-orbit coupling and Hubbard interaction in SrIrO_3 and related Pbnm perovskite oxides*, Phys. Rev. B **86**, 085149 (2012).
- [13] S. Okamoto, *Doped Mott Insulators in (111) Bilayers of Perovskite Transition-Metal Oxides with a Strong Spin-Orbit Coupling*, Phys. Rev. Lett. **110**, 066403 (2013).
- [14] H.-S. Kim, Y. Chen, and H.-Y. Kee, *Surface states of perovskite iridates AlrO_3 : Signatures of a topological crys-*

- talline metal with nontrivial \mathbb{Z}_2 index*, Phys. Rev. B **91**, 235103 (2015).
- [15] Y. Chen, Y.-M. Lu, and H.-Y. Kee, *Topological crystalline metal in orthorhombic perovskite iridates*, Nat. Commun. **6**, 6593 (2015).
- [16] Y. F. Nie, P. D. C. King, C. H. Kim, M. Uchida, H. I. Wei, B. D. Faeth, J. P. Ruf, J. P. C. Ruff, L. Xie, X. Pan, C. J. Fennie, D. G. Schlom, and K. M. Shen, *Interplay of Spin-Orbit Interactions, Dimensionality, and Octahedral Rotations in Semimetallic $SrIrO_3$* , Phys. Rev. Lett. **114**, 016401 (2015).
- [17] Z. T. Liu, M. Y. Li, Q. F. Li, J. S. Liu, W. Li, H. F. Yang, Q. Yao, C. C. Fan, X. G. Wan, Z. Wang, and D. W. Shen *Direct observation of the Dirac nodes lifting in semimetallic perovskite $SrIrO_3$ thin films*, Sci. Rep. **6**, 30309 (2016).
- [18] J.-M. Carter and H.-Y. Kee, *Microscopic theory of magnetism in $Sr_3Ir_2O_7$* , Phys. Rev. B **87**, 014433 (2013).
- [19] S. Tanuma, C. J. Powell, and D. R. Penn, *Calculations of electron inelastic mean free paths. II. Data for 27 elements over the 50-2000 eV range*, Surf. Interface anal. **17**, 911 (1991); *Calculations of electron inelastic mean free paths. V. Data for 14 organic compounds over the 50-2000 eV range*, **21**, 165 (1994).
- [20] A. Sekiyama, T. Iwasaki, K. Matsuda, Y. Saitoh, Y. Ōnuki, and S. Suga, *Probing bulk states of correlated electron systems by high-resolution resonance photoemission*, Nature (London) **403**, 396 (2000).
- [21] A. Yamasaki, Y. Matsui, S. Imada, K. Takase, H. Azuma, T. Muro, Y. Kato, A. Higashiya, A. Sekiyama, S. Suga, M. Yabashi, K. Tamasaku, T. Ishikawa, K. Terashima, H. Kobori, A. Sugimura, N. Umeyama, H. Sato, Y. Hara, N. Miyagawa, and S. I. Ikeda, *Electron correlation in the FeSe superconductor studied by bulk-sensitive photoemission spectroscopy*, Phys. Rev. B **82**, 184511 (2010).
- [22] J. J. Yeh and I. Lindau, *Atomic subshell photoionization cross sections and asymmetry parameters: $1 \leq Z \leq 103$* , At. Data Nucl. Data Tables **32**, 1 (1985).
- [23] A. Sekiyama, S. Kasai, M. Tsunekawa, Y. Ishida, M. Sing, A. Irizawa, A. Yamasaki, S. Imada, T. Muro, Y. Saitoh, Y. Ōnuki, T. Kimura, Y. Tokura, and S. Suga, *Technique for bulk Fermiology by photoemission applied to layered ruthenates*, Phys. Rev. B **70**, R060506 (2004).
- [24] M. Yano, A. Sekiyama, H. Fujiwara, T. Saita, S. Imada, T. Muro, Y. Ōnuki, and S. Suga, *Three-Dimensional Bulk Fermiology of $CeRu_2Ge_2$ in the Paramagnetic Phase by Soft X-Ray $h\nu$ -Dependent (700-860 eV) ARPES*, Phys. Rev. Lett. **98**, 036405 (2007).
- [25] Q. Wang, Y. Cao, J. A. Waugh, S. R. Park, T. F. Qi, O. B. Korneta, G. Cao, and D. S. Dessau, *Dimensionality-controlled Mott transition and correlation effects in single-layer and bilayer perovskite iridates*, Phys. Rev. B **87**, 245109 (2013).
- [26] L. Moreschini, S. Moser, A. Ebrahimi, B. Dalla Piazza, K. S. Kim, S. Boseggia, D. F. McMorrow, H. M. Rønnow, J. Chang, D. Prabhakaran, A. T. Boothroyd, E. Rotenberg, A. Bostwick, and M. Grioni, *Bilayer splitting and wave functions symmetry in $Sr_3Ir_2O_7$* , Phys. Rev. B **89**, R201114 (2014).
- [27] M. K. Crawford, M. A. Subramanian, R. L. Harlow, J. A. Fernandez-Baca, Z. R. Wang, and D. C. Johnston, *Structural and magnetic studies of Sr_2IrO_4* , Phys. Rev. B **49**, 9198 (1994).
- [28] R. J. Cava, B. Batlogg, K. Kiyono, H. Takagi, J. J. Krawski, W. F. Peck, Jr., L. W. Rupp, Jr., and C. H. Chen, *Localized-to-itinerant electron transition in $Sr_2Ir_{1-x}Ru_xO_4$* , Phys. Rev. B **49**, 11890 (1994).
- [29] G. Cao, J. Bolivar, S. McCall, J. E. Crow, and R. P. Guertin, *Weak ferromagnetism, metal-to-nonmetal transition, and negative differential resistivity in single-crystal Sr_2IrO_4* , Phys. Rev. B **57**, R11039 (1998).
- [30] G. Cao, Y. Xin, C. S. Alexander, J. E. Crow, P. Schlottmann, M. K. Crawford, R. L. Harlow, and W. Marshall, *Anomalous magnetic and transport behavior in the magnetic insulator $Sr_3Ir_2O_7$* , Phys. Rev. B **66**, 214412 (2002).
- [31] S. Fujiyama, K. Ohashi, H. Ohsumi, K. Sugimoto, T. Takayama, T. Komesu, M. Takata, T. Arima, and H. Takagi, *Weak antiferromagnetism of $J_{\text{eff}} = 1/2$ band in bilayer iridate $Sr_3Ir_2O_7$* , Phys. Rev. B **86**, 174414 (2012).
- [32] Y. Saitoh, Y. Fukuda, Y. Takeda, H. Yamagami, S. Takahashi, Y. Asano, T. Hara, K. Shirasawa, M. Takeuchi, T. Tanaka, and H. Kitamura, *Performance upgrade in the JAEA actinide science beamline BL23SU at SPring-8 with a new twin-helical undulator*, J. Synchrotron Rad. **19**, 388 (2012).
- [33] See Supplemental Material in Appendix Section for more details.
- [34] The photoelectron escape depth λ in the RP-iridates was found to be about 14 Å at $h\nu \simeq 750$ eV using the TPP-2M formula [19]. The Δk_z was then roughly estimated from $\lambda \cdot \Delta k_z \approx 1/2$ based on the Heisenberg uncertainty relation.
- [35] In producing the constant-energy surfaces, we chose the E_{BS} , where the angle-integrated photoemission spectrum of each RP-iridate had the same normalized intensity (see Supplemental Material).
- [36] P. Blaha, K. Schwarz, G. K. H. Madsen, D. Kvasnicka, and J. Luitz, *WIEN2k, An Augmented Plane Wave + Local Orbitals Program for Calculating Crystal Properties* (Karlheinz Schwarz, Techn. Universität Wien, Austria, 2001).
- [37] The k -mesh of $(10 \times 10 \times 10)$ in the first BZ and the muffin-tin radii of 2.23, 1.97, 1.74 bohr for Sr, Ir, and O were used, being the same as in Ref. [38]. Overall feature in our calculated dispersion relation is quite similar to the reported one in Ref. [16].
- [38] R. Arita, J. Kuneš, A. V. Kozhevnikov, A. G. Eguiluz, and M. Imada, *Ab initio Studies on the Interplay between Spin-Orbit Interaction and Coulomb Correlation in Sr_2IrO_4 and Ba_2IrO_4* , Phys. Rev. Lett. **108**, 086403 (2012).
- [39] N. W. Ashcroft and N. D. Mermin, in *Solid State Physics* (Saunders College Publishing, Fort Worth, 1976), p. 38.
- [40] C. Kittel, in *Introduction to Solid State Physics 7th ed.* (John Wiley & Sons, Inc., New York, 1996), p. 244.
- [41] D. L. Feng, C. Kim, H. Eisaki, D. H. Lu, A. Damascelli, K. M. Shen, F. Ronning, N. P. Armitage, N. Kaneko, M. Greven, J.-i. Shimoyama, K. Kishio, R. Yoshizaki, G. D. Gu, and Z.-X. Shen, *Electronic excitations near the Brillouin zone boundary of $Bi_2Sr_2CaCu_2O_{8-\delta}$* , Phys. Rev. B **65**, R220501 (2002).
- [42] S. Suga, A. Sekiyama, H. Fujiwara, Y. Nakatsu, T. Miyamachi, S. Imada, P. Baltzer, S. Niitaka, H. Takagi, K. Yoshimura, M. Yabashi, K. Tamasaku, A. Higashiya, and T. Ishikawa, *Do all nuclei recoil on photoemission in compounds?*, New J. Phys. **11**, 073025 (2009).

- [43] The χ_o never fits to the experimental data as far as the inner potential V_0 changes within any realistic values ($0 \leq V_0 \leq 30$ eV).
- [44] M. Uchida, Y. F. Nie, P. D. C. King, C. H. Kim, C. J. Fennie, D. G. Schlom, and K. M. Shen, *Correlated vs. conventional insulating behavior in the $J_{\text{eff}} = 1/2$ vs. $3/2$ bands in the layered iridate $Ba_2\text{IrO}_4$* , Phys. Rev. B **90**, 075142 (2014).
- [45] Judging from our calculated results, the band originates from the $j_{\text{eff}}=3/2$ ($j_z=\pm 1/2$) band although it was assigned to the $j_{\text{eff}}=1/2$ band.
- [46] H. Watanabe, T. Shirakawa, and S. Yunoki, *Microscopic Study of a Spin-Orbit-Induced Mott Insulator in Ir Oxides*, Phys. Rev. Lett. **105**, 216410 (2010).
- [47] For instance, one can find only one band at Γ point in the result at $h\nu=85$ eV (see Table II) since the dispersion along $(\pi,\pi)-(\pi,0)$ is probably displayed as that along the Γ -M line.
- [48] We measured the ARPES spectra above T_N both at the end of the heating process and at the start of the cooling process after cleaving the crystal. These spectra showed good reproducibility.
- [49] J. Braun, J. Minár, S. Mankovsky, V. N. Strocov, N. B. Brookes, L. Plucinski, C. M. Schneider, C. S. Fadley, and H. Ebert, *Exploring the XPS limit in soft and hard x-ray angle-resolved photoemission using a temperature-dependent one-step theory*, Phys. Rev. B **88**, 205409 (2013).
- [50] N. J. Shevchik, *Disorder effects in angle-resolved photoelectron spectroscopy*, Phys. Rev. B **16**, 3428 (1977).
- [51] P. D. C. King, T. Takayama, A. Tamai, E. Rozbicki, S. McKeown Walker, M. Shi, L. Patthey, R. G. Moore, D. Lu, K. M. Shen, H. Takagi, and F. Baumberger, *Spectroscopic indications of polaronic behavior of the strong spin-orbit insulator $\text{Sr}_3\text{Ir}_2\text{O}_7$* , Phys. Rev. B **87**, R241106 (2013).
- [52] J.-M. Carter, V. Vijay Shankar, and H.-Y. Kee, *Theory of metal-insulator transition in the family of perovskite iridium oxides*, Phys. Rev. B **88**, 035111 (2013).

Appendix A: Detailed experimental conditions

The detailed experimental conditions used in the soft-x-ray (SX) angle-resolved photoemission spectroscopy (ARPES) of Ruddlesden-Popper-type iridium oxides (RP-iridates) are summarized in Table III. To obtain the electronic structures in the k_x - k_y plane, emission-angle(ξ)-dependent spectra were measured at a fixed angle θ , where ξ is defined as the angle formed between the direction directly toward the electron-energy analyzer and the emission direction of a photoelectron detected through the entrance slit of the analyzer, and θ is the angle between the directions toward the analyzer and normal to the sample surface. The analyzer was designed such that the range of ξ was set to be $\pm 6^\circ$. The dataset of the photoelectron intensity $I(\xi, \theta, E_k)$ was acquired by scanning θ , and then, converted to, for in-

stance, $I(k_x, k_y, E_B)$ using the following formulae:

$$k_x = \frac{\sqrt{2mE_k}}{\hbar} \sin \xi, \quad (\text{A1})$$

$$k_y = \frac{\sqrt{2mE_k}}{\hbar} \sin \theta - q_{\parallel}, \quad (\text{A2})$$

$$E_B = h\nu - W - E_k, \quad (\text{A3})$$

where E_k , E_B , $h\nu$, and W indicate the kinetic energy of the photoelectron, the binding energy of the emitted electron in the initial state, the photon energy, and the work function, respectively. q_{\parallel} ($= |\mathbf{q}| \cos 45^\circ$ in the present study) is the photon momentum parallel to the sample surface. Here, we assume the free-electron final state. Meanwhile, the electronic structures along the k_z axis were obtained by scanning the excitation photon energy. The dataset corresponding to $I(\xi, h\nu, E_k)$ at a fixed angle θ was converted to, for instance, $I(k_x, k_z, E_B)$ by Eqs.(A1)-(A3), and

$$k_z = \sqrt{\frac{2m(E_k + V_0)}{\hbar^2} - (k_x^2 + k_y^2)} + q_{\perp}, \quad (\text{A4})$$

where q_{\perp} is the photon momentum perpendicular to the sample surface, and V_0 is the inner potential, which is a fitting parameter used in the present study.

Appendix B: Estimation of inner potential V_0

As shown in Figs. 8(a)-(c), a Brillouin zone (BZ) shifts relative to the constant-energy surface depending on the inner potential V_0 . For SrIrO_3 (Sr113), it is obvious that the best-fit value of V_0 occurs at about 10 eV within any realistic value ($0 \leq V_0 \leq 30$ eV). In contrast, it is difficult to optimize the V_0 for $\text{Sr}_3\text{Ir}_2\text{O}_7$ (Sr327) and Sr_2IrO_4 (Sr214) since the electronic structures along the k_z axis in Sr327 do not follow the periodicity of the BZ because of the k_z -dependent oscillation resulting from the bilayer coupling, while in Sr214, they are almost structureless because of the layered crystal structure. We estimated the V_0 of Sr327 to be 18 eV, where the electronic structure around a k_z point, indicated as ‘‘T’’ shown in Fig. 8(b), is symmetric about the determined high-symmetry line X- Γ -X. As a consequence, the waveform of the bilayer coupled oscillation is well-reproduced by the calculation shown in Fig. 5(b). In Sr214, we found a slight deformation in the constant-energy surface at $E_B=1.0$ eV, as shown in Fig. 8(c). To fit the BZ to the deformed surface, a V_0 value of about 27 eV was used for Sr214.

Appendix C: Determination of binding energies for producing constant-energy surfaces

Figure 9 shows the photoemission spectra obtained by summing up the k -resolved spectra in both k_x - k_y and k_{\parallel} - k_z planes shown in Figs. 1(d)-(i). We referred the spectra

TABLE III: Detailed conditions of SX-ARPES experiments for RP-iridates. Regarding the sample configuration, the axis of the θ rotation is parallel to the entrance slit of the electron-energy analyzer. $\theta=0$ indicates the normal emission of the photoelectrons. Note that it does not correspond to k_x (and/or k_y) = 0 because of the momentum transfer from a photon to the photoelectron. ϕ and ψ are the azimuth and tilting angles of the sample stage.

| Compound | Mapping or band dispersion | Photon energy (eV) | θ, ϕ, ψ ($^\circ$) | Temperature (K) | Displayed in Figure(s) |
|--|----------------------------|--------------------|-----------------------------------|-----------------|---------------------------------------|
| SrIrO ₃ (without capping layer) | Γ -X-M-X | 730 | -5.0 to +6.0, 0, 0 | 20 | 1(g) |
| | Γ -X | 730 | -0.7, 0, 0 | 20 | 2(b), 3(a) |
| | X-M | 730 | -3.8, 0, 0 | 20 | 11(b) |
| | X-M-R-M | 650 | -5.0 to +6.0, 0, 0 | 20 | 4(a) |
| | X-M | 650 | -1.0, 0, 0 | 20 | 3(a), 3(d), 3(e), 10(b), 11(a) |
| | M-R | 650 | -4.1, 0, 0 | 20 | 3(a) |
| | Γ -X-M-X | 575-910 | -0.5, 0, 0 | 20 | 1(d), 8(a) |
| SrIrO ₃ (with capping layer) | Γ -M | 730 | 2.0, 45, 0 | 20 | 3(a), 3(d), 3(e), 10(a) |
| | Γ -R | 880 | -5.3, 35, 45 | 20 | 3(a), 3(d), 3(f), 10(d), 10(e), 10(f) |
| | Γ -R | 880 | -7.0 to -1.0, 35, 45 | 20 | 10(g) |
| | X-R | 810 | 2.0, 45, 0 | 20 | 3(a), 3(d), 3(f), 10(c) |
| | Γ -X-R-M | 550-900 | 2.0, 45, 0 | 20 | 1(d), 10(e) |
| Sr ₃ Ir ₂ O ₇ | Γ -M-X-M | 769 | -6.0 to +5.0, 0, 0 | 100 | 1(h) |
| | Γ -M | 845 | -1.0, 0, 0 | 100 | 2(c), 3(b) |
| | M-X | 845 | -3.7, 0, 0 | 100 | 3(b) |
| | Γ -X | 855 | 0.6 ^a , 45, 0 | 100 | 3(b) |
| | Γ -X-X-Z | 650-995 | -0.6 ^a , 45, 0 | 100 | 1(e), 5(a), 5(b), 8(b) |
| | Γ -M-M-Z | 710-900 | -1.0, 0, 0 | 100 | 1(e) |
| | M | 689 | -1.0, 0, 0 | 78, 300 | 7(b) |
| Sr ₂ IrO ₄ | Γ -M-X-M | 760 | -6.3 to 5.1, 0, 0 | 78 | 1(i), 6(f) |
| | Γ -M | 760 | -0.7, 0, 0 | 78 | 2(a), 2(d), 3(c) |
| | M-X | 760 | -3.9, 0, 0 | 78 | 2(a), 3(c) |
| | Γ -X | 405 | -1.0, 45, 0 | 100 | 2(a), 3(c), 12(a), 12(e) |
| | Γ -X | 760 | -0.8, 45, 0 | 100 | 6(e), 12(b), 12(f) |
| | Γ -X | 812 | -1.0, 45, 0 | 100 | 12(c), 12(g) |
| | Γ -X | 838 | -0.8, 45, 0 | 100 | 12(d), 12(h) |
| | Γ -X-X-Z | 690-900 | -1.0, 45, 0 | 100 | 1(f), 8(c) |
| | M | 760 | -0.7, 0, 0 | 78, 300 | 7(b) |

^aThese data were acquired from different crystal grains in a series of measurements.

to produce the constant-energy surfaces in Figs. 1(e), (f), (h), and (i). The values of E_B in these figures were chosen such that the spectral intensities of Sr327 or Sr214 at E_B was similar to that of Sr113 at the Fermi energy (E_F), as indicated by the dotted lines in Fig. 9.

Appendix D: Estimation of Fermi velocity and Fermi wavenumber

Figures 10(a)-(d) show momentum-distribution curves of Sr113 in the vicinity of E_F . We used one (two) Gaussian function(s) to reproduce the curves along the Γ -M and X-R (M-X and R- Γ) lines, in addition to a Lorentzian-type background function if necessary. The estimated peak position indicated by the vertical bar significantly shifts with the binding energy in the X-M and

X-R lines. Meanwhile, the shift is not well-resolved in the Γ -M and R- Γ lines because of the large v_F values.

The momentum-distribution curve at E_F along the R- Γ line is shown in Fig. 10(e) (in red); this was obtained using the measurement with high energy resolution and high statistics. The cross-sectional curve of the mapped Fermi surface in the k_z - $k_{||}$ plane is depicted in blue. Compared to the blue line, the intensity of the red line on the negative side of the k axis is strongly suppressed due to the matrix element effect. Nevertheless, the R point should be correctly assigned since the two E_F -crossing points and a parabolic band centered at the R point are clearly resolved in Fig. 10(f). In addition, Fig. 10(g) shows that the band maximum of the parabolic band was also located at the assigned R point in the other axis perpendicular to the horizontal axis in Fig. 10(f), demonstrating a genuine high-symmetry point.

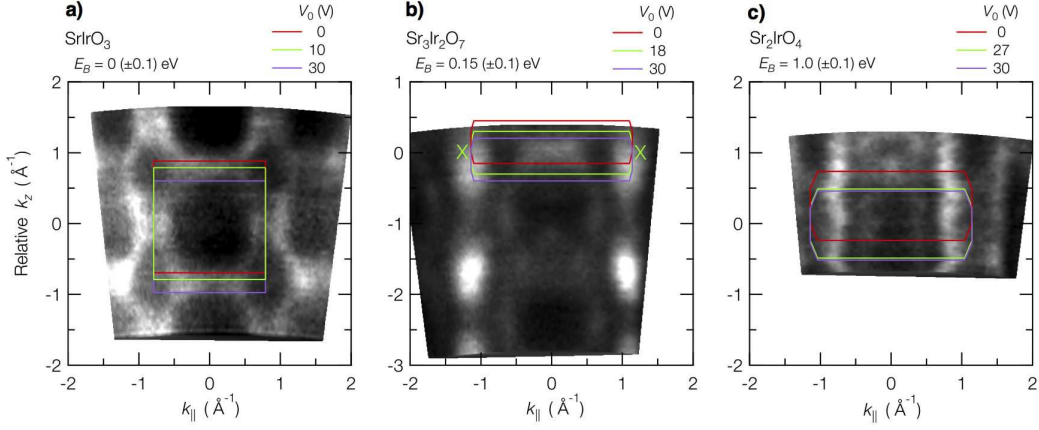


FIG. 8: Constant-energy surfaces along the k_z axis in (a) Sr113, (b) Sr327, and (c) Sr214. The cross-sectional views of the BZs are displayed by solid lines.

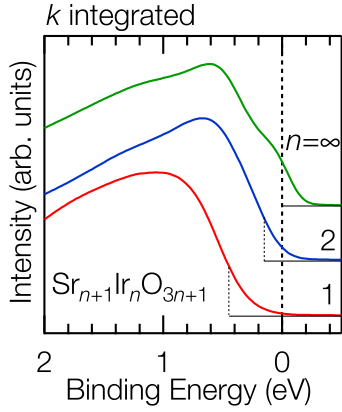


FIG. 9: Referenced photoemission spectra of RP-iridates.

Appendix E: Visible energy bands at different photon energies

Figures 11(a) and (b) show the energy-band dispersions along the X-M line in the Sr113 measured at two different photon energies. One can see the widely dispersive band in the $E_B=1-2$ eV range at $h\nu=730$ eV, which are not resolved at 650 eV. In contrast, the characteristic feature in the vicinity of E_F is more clearly seen at $h\nu=650$ eV.

Appendix F: Deformation of Fermi surface

As listed in Table IV, we have obtained the Fermi wavenumber k_F of Sr113 from the ARPES spectra and LDA+SOC calculations shown in Figs. 3(e) and (f). Experimental k_F values are generally closer to the values in TB model than to those in LDA+SOC calculations.

TABLE IV: Fermi wavenumber k_F along high-symmetry lines in Sr113. k_F is defined as the distance from the point M (R) in the X-M and M- Γ (Γ -R and R-X) lines. The value in square brackets represents the deviation from k_F in each high-symmetry line of the experimental FS listed at the top of the Table.

| | high-symmetry line in cubic BZ | k_F (\AA^{-1}) |
|----------|-----------------------------------|--------------------------------|
| SX-ARPES | X - M | 0.37 |
| | M - Γ | 0.48 |
| | Γ - R | 0.63 |
| | R - X | 0.71 |
| LDA+SOC | X - M | 0.48 [130%] |
| | M - Γ | 0.32 [67 %] |
| | Γ - R | 0.56 [89 %] |
| | R - X | 0.87 [122%] |
| TB model | X - M | $\pi/2a$ [107%] |
| | M - Γ | $\sqrt{2}\pi/3a$ [78 %] |
| | Γ - R | $\sqrt{3}\pi/2a$ [108%] |
| | R - X | $2\sqrt{2}\pi/3a$ [104%] |

Appendix G: $h\nu$ -dependence of photoelectron intensity in folded and unfolded j_{eff} bands

Figures 12(a)-(h) show the energy-band dispersions along the Γ -X line in the Sr214 measured at various photon energies. To investigate the influence of the photon-energy variation on the photoelectron intensity in some j_{eff} bands, we focused on three points named A, B, and C, indicated by arrows in Fig. 12(e). The bands to which points A and C belong are assigned to the folded and unfolded $j_{\text{eff}}=3/2$ bands, respectively, predicted by calcu-

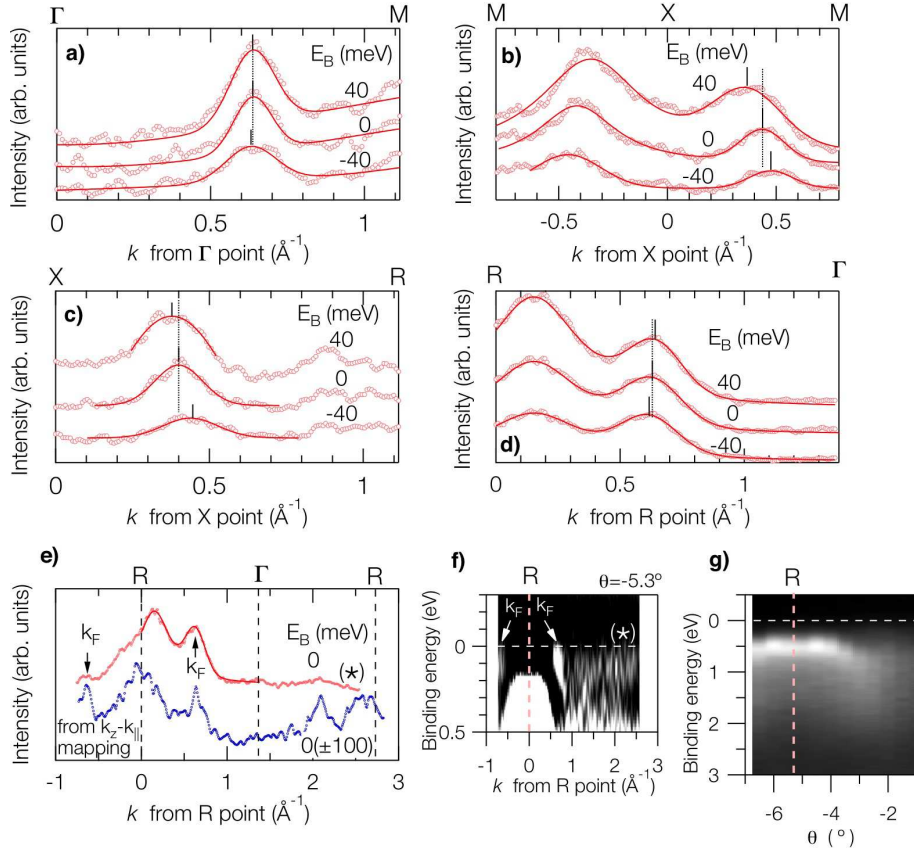


FIG. 10: Estimation of peak positions in momentum-distribution curves along the (a) Γ -M, (b) X-M, (c) X-R, and (d) R- Γ lines in Sr113. Only some examples of the curves in the vicinity of E_F are shown. To fit the experimental data, one or two Gaussian functions, and if necessary, a background Lorentzian function were used. (e) Momentum-distribution curves at E_F extracted from the ARPES spectrum partly shown in Fig. 3(f) and from the constant-energy surface in Fig. 1(d). (f) The second-derivative image of the ARPES spectrum along the R- Γ line. The momentum-distribution curve denoted by (*) in (e) corresponds to the data indicated by the broken line at E_F . (g) Energy-band dispersion along the θ axis, which is perpendicular to the horizontal axis in (f).

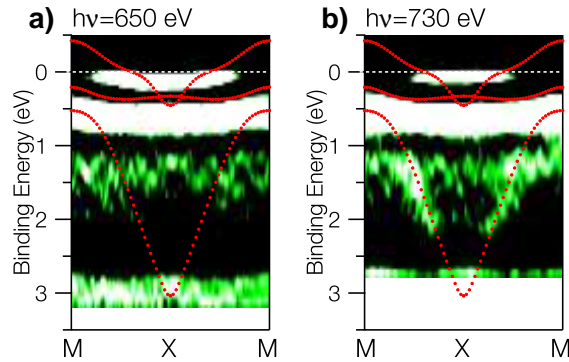


FIG. 11: Energy-band dispersion along the X-M line in Sr113 measured at two different photon energies: (a) 650 eV and (b) 730 eV. The second-derivative images yield a better view of the dispersions. The LDA+SOC band structure of cubic Sr113 is also shown by dots.

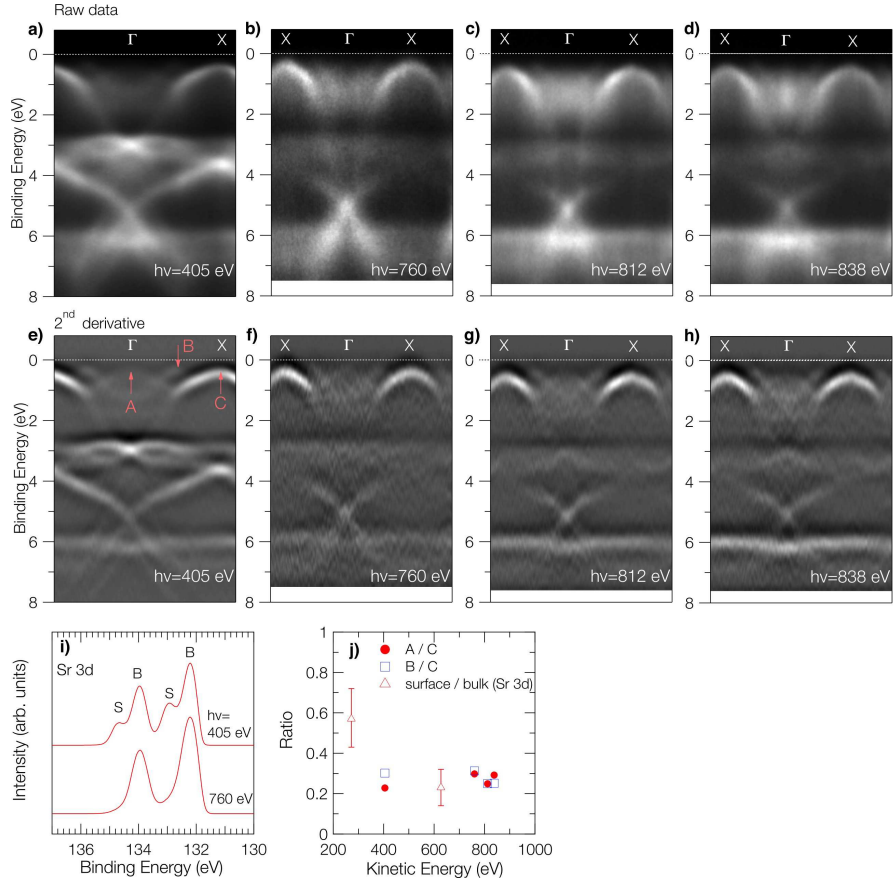


FIG. 12: Energy-band dispersions of Sr214 measured at various photon energies: (a)-(d) photoelectron-intensity distributions and (e)-(h) their second-derivative images. (i) Sr 3d core-level photoemission spectra at $h\nu=405$ and 760 eV. “B” and “S” denote the peaks originating from the electronic states in the bulk and on the surface, respectively. (j) The ratio of the photoelectron intensity at point Γ in a folded $j_{\text{eff}}=3/2$ band [“A” in (e)] to that at point X in the original unfolded band (“C”). The ratio between the intensities around $(\pi/2, \pi/2, 0)$ in the $j_{\text{eff}}=1/2$ band (“B”) and at the X point in the $j_{\text{eff}}=3/2$ band is also shown.

lations based on the three-orbital Hubbard model. The band including point B is predicted in both the folded and unfolded BZ pictures. As seen in Fig. 12(j), photoelectron intensities at points A and B relative to point C are independent of the kinetic energy of the photoelectrons. The surface spectral weight relative to the bulk

weight estimated from the Sr 3d core-level photoemission spectrum in Fig. 12(i) is also shown, clearly indicating that the surface components are suppressed with increasing photon energy, because of the variation in bulk sensitivity.